Electromagnetically Modified Filtration of Aluminum Melts—Part I: Electromagnetic Theory and 30 PPI Ceramic Foam Filter Experimental Results

MARK WILLIAM KENNEDY, SHAHID AKHTAR, JON ARNE BAKKEN, and RAGNHILD E. AUNE

In the present work, laboratory-scale continuous filtration tests of liquid A356 aluminum alloy have been performed. The tests were conducted using standard 30 PPI (pores per inch) ceramic foam filters combined with magnetic flux densities (~0.1 and 0.2 T), produced using two different induction coils operated at 50 Hz AC. A reference filtration test was also carried out under gravity conditions, *i.e.*, without an applied magnetic field. The obtained results clearly prove that the magnetic field has a significant affect on the distribution of SiC particles. The influence of the electromagnetic Lorentz forces and induced bulk metal flow on the obtained filtration efficiencies and on the wetting behavior of the filter media by liquid aluminum is discussed. The magnitudes of the Lorentz forces produced by the induction coils are quantified based on analytical and COMSOL 4.2® finite element modeling.

DOI: 10.1007/s11663-013-9798-8

I. INTRODUCTION

A typical aluminum melt normally contains a large number of small non-metallic inclusion particulates, less than or equal to 50 μm in size. These include particles of oxides (Al_2O_3), spinels ($MgO{\cdot}Al_2O_3$), and carbides (SiC, Al_4C_3), with a higher melting point than the host metal. The presence of these inclusions in the aluminum melt not only reduces the static and dynamic mechanical properties of the material but also decreases the corrosion resistance and has detrimental effects on the surface finish of the end product. Non-metallic inclusions can also act as nucleation sites for hydrogen porosity.[1] Remelting of post-consumed and process aluminum scrap also reveals new challenges not only in relation to environmental issues but also with respect to the metal yield and quality.

Removal of inclusions from liquid aluminum alloys is today an important melt treatment process. The increasing demand for high purity aluminum components to be used in the automotive and aviation industry, as well as for construction and electrical purposes, has put a strain on the manufacturers to produce cleaner aluminum. Attention is therefore being given to finding new or improved processes and/or process routes for the removal of non-metallic inclusions from aluminum melts.[2]

Many different methods for the removal of inclusions from molten aluminum already exist, *i.e.*, (i) settling, (ii) flotation, (iii) degassing, and (iv) liquid metal filtration. Each of these methods is capable of removing a size range of inclusions, but the methods are generally ineffective at removing inclusions of <10 μm and each have unique process limitations.[3]

The filtration process has a complex mechanism influenced by hydrodynamic factors such as fluid flow, turbulence, surface and body forces, as well as chemical and metallurgical interactions between the inclusions, the filter media, and the liquid metal. These filtration mechanisms are not thoroughly understood and deeper theoretic and experimental analyses are needed to explore the potential for improving the cleaning efficiency of the filter media.[4] In the aluminum filtration process, the most frequently used filter media are ceramic foam filters (CFFs).

The principle of electromagnetic separation by Lorentz forces ($\mathbf{J} \times \mathbf{B}$) was described mathematically in 1954 by Leenov and Kolin.[5] A schematic representation of the Lorentz forces and the reaction forces acting on a non-conducting particle in a curl-free magnetic field is presented in Figure 1. Figure 1 does not represent the geometry used in the current work, but is meant to be illustrative of the electromagnetic principles applied. In this concept, non-conductive particles migrate through the melt in a direction opposite to the Lorentz forces produced by the cross product of a homogeneous magnetic field and a uniform current distribution. The non-conductive particles present in the fluid will expe-

MARK WILLIAM KENNEDY, PhD Candidate, is with the Department of Material Science and Engineering, Norwegian University of Science and Technology (NTNU), 7491 Trondheim, Norway and Chief Technology Officer, Proval Partners S.A., 1004 Lausanne, Switzerland. Contact e-mail: m.kennedy@provalp.com SHAHID AKHTAR, Technical Manager, is with the Hydro Aluminium, Karmøy, 4265 Håvik, Norway. JON ARNE BAKKEN, Professor Emeritus, is with the Department of Material Science and Engineering, Norwegian University of Science and Technology (NTNU). RAGNHILD E. AUNE, Professor, is with the Department of Material Science and Engineering, Norwegian University of Science and Technology (NTNU) and also with the Department of Material Science and Engineering, Royal Institute of Technology (KTH), 100 44 Stockholm, Sweden.

Manuscript submitted December 2, 2011.
Article published online February 6, 2013.

rience a pressure gradient created by the Lorentz forces, but not the Lorentz forces themselves. This will cause the particles to migrate in a direction counter to the Lorentz forces. An early example of the application of this technique was reported in 1968 by Vilinskas and Schiltz,[6] *i.e.*, the removal of zirconium oxide spheres from liquid sodium. Various methods of applying this principle in metallurgical processing were patented by Conti *et al.* in 1989.[7]

There are several studies reported in the literature illustrating the migration of oxide and SiC inclusions under the influence of electromagnetic fields.[8–12] Based on metallographic examinations, it has been established that in the presence of an electromagnetic field, the particles are collected into the stagnant hydrodynamic boundary layers. While the potential of this innovative method has been demonstrated in small batch tests, its implementation in industrial application under continuous flow conditions has not been reported for aluminum. A significant problem at present is that powerful and curl-free Lorentz forces are difficult to achieve in industrial practice.[13]

In 1990, El-Kaddah *et al.*[14,15] presented the concept of combining electromagnetic separation with filtration to control secondary mixing effects and to enhance the inclusion removal efficiency. Sufficient experimental verification of this concept was, however, not provided at that time. A more recent patent application on the use of flow modifying devices of a high collection area has been filed by other researchers.[16]

The current authors have recently shown that the melt circulation through the filter media is driven by the strong curl present in the Lorentz forces.[17] A figure indicating the electromagnetic field and Lorentz forces present in the filtration apparatus used in these experiments (as modeled with the commercial finite element code COMSOL 4.2®) is shown in Figure 2. If a standard induction coil of constant pitch is used in such an experiment, a large curl is always present in the Lorentz forces due to strong coil end effects (*i.e.*, practical coils are not infinite in length). The magnitude of the curl in the experimental apparatus is increased by the reduced effective electrical conductivity of the filter element itself.

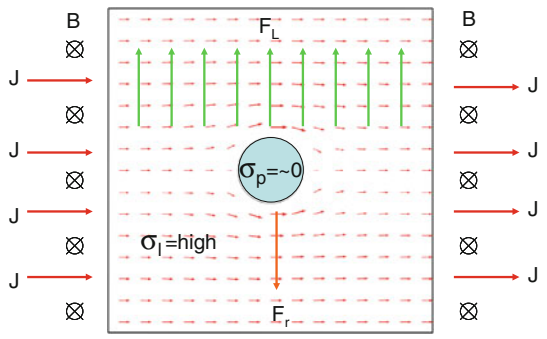

Fig. 1—The Lorentz forces (F_L) and the reaction forces (F_r) acting on a non-conducting particle in a curl-free magnetic field. Note the impact of the particulate on the current distribution (J = current density (A/m^2); B = magnetic flux density (T); σ_l = liquid phase electrical conductivity (S/m); σ_p = particulate electrical conductivity (S/m)).

For the 30 PPI filters used in these experiments, there is ~50 pct higher electrical resistance or 33 pct lower effective electrical conductivity inside of the filter due to the obstructions (tortuosity) and reduced conducting area (porosity), as has recently been reported elsewhere.[18] In Figure 2, the impact of the variable "effective" electrical conductivity between the metal and filter regions is very clearly indicated by the shape and intensity of the electromagnetic field and the resulting magnitude of the Lorentz forces produced, as indicated by the length of the arrows. The resulting curl is figuratively illustrated by the rotating dotted circle.

With strong melt flow driven by the Lorentz forces, it was expected that the melt recirculation and not the *Leenov-Kolin "pinch" effect* would dominate the distribution of the particles over, within, and under the filters used in these experiments. Only at the outer wall, where velocities are low (*i.e.*, in the hydrodynamic boundary layer) and the Lorentz forces are maximized, is it reasonable to assume that magnetic particle migration may occur under the influence of the "pinch" effect.

In the present study, an experimental setup was designed for laboratory-scale continuous filtration flow testing. The tests were conducted with standard 30 PPI CFFs under the influence of a magnetic flux density of ~0.1 and 0.2 T. One reference gravity flow test was also conducted for comparison. A new analytical expression of the time average Lorentz forces will be presented and

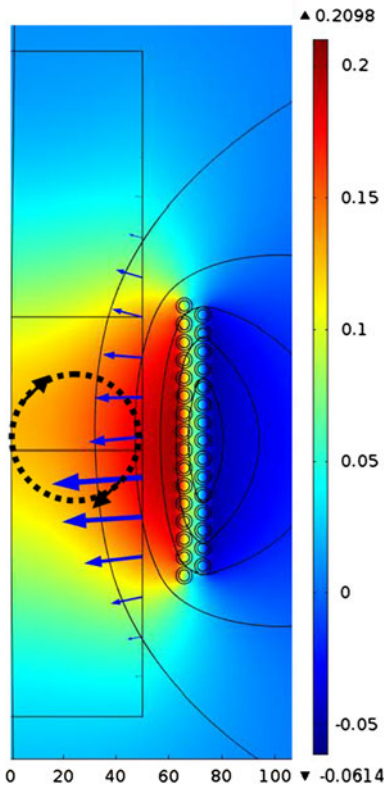

Fig. 2—Actual experimental geometry showing a COMSOL 4.2® simulation of the RMS magnetic flux density (T) as well as the relative magnitude of the Lorentz forces acting on the surface of the test samples (solid arrows) for Coil #2. The direction of the expected bulk aluminum circulation is marked as a dotted circle with arrows.

compared with finite element modeling using COMSOL 4.2®. The filter elements used in the filtration flow tests were characterized using standard metallographic techniques. Overall quantitative filtration efficiency and efficiency as a function of particle size are reported for gravity reference and high field strength conditions using a computerized macro-automated photographic particle analysis technique.

II. THEORY

Leenov and Kolin[5] derived the following equation describing the reaction force acting on a low conductivity particle present in a high conductivity fluid when subjected to a curl-free Lorentz force field:

$$\mathbf{F}_r = -\frac{3}{2}\frac{\sigma_l - \sigma_p}{2\sigma_l + \sigma_p}\frac{\pi d_p^3}{6}\mathbf{F}_L \quad [1]$$

where $\mathbf{F}_r$ is the reaction force experienced by the particulate (N), $\mathbf{F}_L$ is the Lorentz force acting on the fluid (N/m^3), σ_l is the electrical conductivity of the liquid phase (S/m), σ_p is the particle electrical conductivity (S/m), and d_p is the particle diameter (m). For non-conducting particles, Eq. [1] can be reduced to the following:

$$\mathbf{F}_r = -\frac{\pi d_p^3}{8}\mathbf{F}_L \quad [2]$$

where

$$\mathbf{F}_L = \mathbf{J} \times \mathbf{B} \quad [3]$$

assuming that

$$\nabla \times \mathbf{F}_L = 0 \quad [4]$$

It is a well-known fact that a curl-free Lorentz force field can be effectively produced by combining a homogenous direct current and a non-varying magnetic field working at 90 deg as figuratively illustrated in Figure 1. However, if a curl exists in the Lorentz force field, it will produce electromagnetic or magneto-hydrodynamic (MHD) stirring. This is referred to as the secondary mixing effect, as observed by several investigators.[13,14] These mixing effects result in particles being rapidly transported from the bulk of the melt to the crucible walls (in crucible batch experiments) where the stagnant hydrodynamic boundary layers exist. The particles can then be collected into the boundary layers through the reaction force presented in Eq. [1] or [2]. A limited volume, however, exists within which to accumulate particles and the ability of the particles to resist re-entrainment can be questioned.

In the present study, two different induction coil designs have been used to simultaneously produce (i) a magnetic field, (ii) induce eddy currents to produce resistive heating, and (iii) produce Lorentz forces through the interaction of the magnetic flux density and the induced currents. The eddy current density (**J**) is related to the curl of the magnetic field intensity ($\nabla \times \mathbf{H}$) and the magnetic flux density (**B**) as presented in the following equation:

$$\mathbf{J} = \nabla \times \mathbf{H} = \frac{\nabla \times \mathbf{B}}{\mu} \quad [5]$$

where **J** is the eddy current density (A/m^2), **H** is the magnetic field intensity (A(-turns)/m), **B** is the magnetic flux density (T), and μ is the electromagnetic permeability of the conductive fluid, which is equal to $4\pi \times 10^{-7}$ for aluminum (H/m). Further details related to the magnetic fields produced by "short" solenoidal coils and induction heating can be found elsewhere.[19,20]

Most coils used for induction heating are "short,"[19–21] and have a significant radial and axial variation in their magnetic flux density. This is axially evaluated using the Biot-Savart law[20] and presented in Figure 3 in a dimensionless form. As indicated in Figure 3, a large variation in the magnetic flux density does exist for "short" coils along their z-axis when the diameter to length ratio of the coil (D_c/l_c) lies between 0.3 and 2.0, which are typical values for induction coils.

It is the time-varying value of the local magnetic flux density in the z-direction which induces the current in the liquid metal in the phi direction. It should be pointed out that this is in accordance with Eq. [5]. The variation in the local flux density will result in a similar variation in the local current density. In other words, an axial variation in **H** and **B** will produce a similar variation in **J**. These local variations will then combine to produce a powerful curl in the z-direction of the Lorentz forces, resulting in strong MHD mixing.

Lorentz forces orders of magnitude stronger than the gravity forces can easily be generated using "short" induction coils. This will in turn result in MHD mixing, which will dominate the hydrodynamic flow and cause robust recirculation. The investigation of the curl in the Lorentz forces, and the resulting recirculation of the melt, is the main focus of the present study.

It is important to point out that in Eq. [3], **J** and **B** are both vectors and phasors (time-varying functions) that can be represented by complex vector quantities, *i.e.*, by $\underline{\mathbf{J}}$ and $\underline{\mathbf{B}}$. The phase shift between $\underline{\mathbf{J}}$ and $\underline{\mathbf{B}}$ changes with the penetration depth into the workpiece, making the

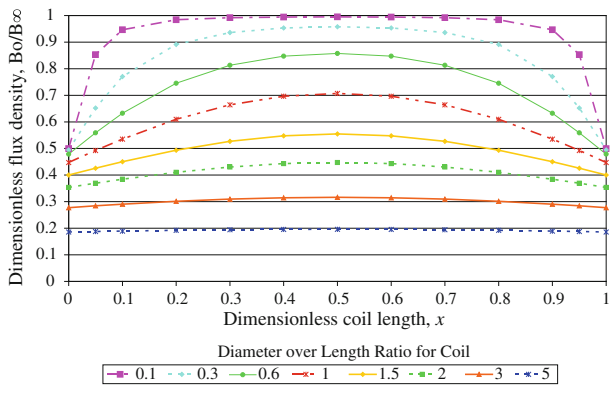

Fig. 3—The dimensionless flux density B_0/B_∞ (z-component) for different coil diameter to length ratios (D_c/l_c) as a function of the dimensionless coil length (x).[20]

solution for the Lorentz forces challenging. The following formula is proposed for the time-averaged values, *i.e.*, the real part of $\underline{\mathbf{J}} \times \underline{\mathbf{B}}$:

$$|\mathbf{F}_L| = \mathrm{Re}\{\underline{\mathbf{J}}^* \times \underline{\mathbf{B}}\} \quad [6]$$

where $\underline{\mathbf{J}}^*$ is the complex conjugate of the root mean square (RMS) current density (scalar values of A/m^2) and $\underline{\mathbf{B}}$ is the RMS complex magnetic flux density (scalar values of T). From the definition of the vector cross product and the right hand rule, the time average force is known to be in the negative r-direction. The Lorentz component in the z-direction is in the present study assumed to be negligible.

Inserting the relevant phi and axial components of **J** and **B** in accordance with Eq. [3] into Eq. [6] and applying the modified zero order Kelvin Bessel functions will result in the following expression for the time-averaged Lorentz forces:

$$F_{\mathrm{RMS}} = -\frac{\mu_r \mu_0}{\delta_l}\left(\frac{k_N^* N_c I_c}{l_c}\right)^2 \varphi(R,r) = -\frac{\mu_r \mu_0}{\delta_l} H_s^2 \varphi(R,r) \quad [7]$$

where μ_r is the relative magnetic permeability with a suggested value of 1.0000 for air, copper, and aluminum (unitless), μ_0 is the magnetic permeability of free space 4×10^{-7} (H/m), k_N^* is the modified short coil correction factor (unitless), N_c is the number of coil turns, I_c is the coil RMS current (A), l_c is the length of the coil (m), φ is a dimensionless correction factor accounting for the magnitude and phase shift of $\underline{\mathbf{J}}$ and $\underline{\mathbf{B}}$ at depth r, δ_l is the electromagnetic penetration depth in the liquid metal (m), and H_s is the average z-component of the surface magnetic field intensity (A(-turn)/m). The negative sign in Eq. [7] indicates an orientation in the negative radial direction. The dimensionless correction factor $\varphi(R,r)$ can be expressed as follows:

$$\varphi(R,r) = \frac{\sqrt{2}(\mathrm{ber}\xi_r \mathrm{ber}'\xi_r + \mathrm{bei}\xi_r \mathrm{bei}'\xi_r)}{\mathrm{ber}^2(\xi_R) + \mathrm{bei}^2(\xi_R)} \quad [8]$$

where ξ_r is the dimensionless reference depth where the Lorentz force is to be evaluated and ξ_R is the dimensionless reference depth at the surface. Ber, ber′, bei, and bei′ are the real and imaginary parts of the zero order modified Kelvin Bessel functions and their derivatives, the solutions to which can be found using numerical solvers[22] or lookup tables.[23] The following is valid for the dimensionless reference depths:

$$\xi_R = \frac{\sqrt{2}R}{\delta_l}, \quad \xi_r = \frac{\sqrt{2}r}{\delta_l} \quad [9]$$

where R is the outer radius (m) and r is the radius at which the Lorentz forces are to be evaluated (m).

For the electromagnetic penetration depth, the following is valid:

$$\delta_l = \left(\frac{\rho_l}{\pi \mu_r \mu_0 f}\right)^{1/2} \quad [10]$$

where ρ_l is the resistivity of the liquid metal (Ω m) and f is the frequency (Hz).

Equations [7] through [10] are similar to the equations previously published by Korovin[24,25]; however, the real and imaginary parts have been separated in Eq. [8]. In the English translations of Korovin's work,[24,25] the real and imaginary parts of his equations were confounded by the accidental omission of the $\sqrt{-1}$ and the resulting equation cannot be used for any practical purpose. The present authors have also modified Eq. [7] to include the frequency adjusted "short" coil correction factor,[20] without which it is not possible to analytically estimate the Lorentz forces with less than about a factor of two errors, *i.e.*,

$$k_N^* = k_N\left(1 - \left(\frac{D_l - \delta_l}{D_c + \delta_c}\right)^2\right) + \left(\frac{D_l - \delta_l}{D_c + \delta_c}\right)^2 \quad [11]$$

where k_N is the "air-core" "short" coil correction factor of Nagaoka,[26] D_l is the outside diameter of the liquid metal (m), D_c is the inside diameter of the coil (m), and δ_c is the electromagnetic penetration depth into the coil (m).

The empirical formula proposed by Knight[27]

$$k_N = \frac{1}{1 + 0.4502\left(\frac{(D_c + \delta_c)}{l_c}\right)} \quad [12]$$

conveniently estimates the "air-core" "short" coil correction factor to ~3 significant digits. It should be pointed out that Eqs. [11] and [12] are one-dimensional correction factors. To compare the analytical results with 2D axial symmetric finite element modeling, a line integral must be calculated at each radial position of interest, *i.e.*, a line taken from the top to the bottom of the coil.

To evaluate Eqs. [7] through [12], it is necessary to estimate the electrical resistivity of the liquid aluminum as a function of temperature. The data of Brandt and Neuer[28] have in the present study been selected for the calculation of the electrical resistivity of the liquid metal. Their data for metal containing 7 wt pct Si and 0.6 wt pct Mg can be represented as follows

$$\rho_l = \rho_0(1 + \alpha_{894}[T - 894\ \mathrm{K}]) \quad [13]$$

where ρ_0 is the resistivity of the liquid metal at the reference temperature T (Ω m), α_{894} is the temperature coefficient of resistivity (K^{-1}), and T is the reference temperature [894 K (621 °C)]. The following values are recommended: $\rho_0 = 2.883 \times 10^{-7}$ Ω m, $\alpha_{894} = 5.59 \times 10^{-4}\ K^{-1}$.[28]

The conductivity of the experimental alloy with additions of SiC and oxide particles can be estimated by dividing Eq. [13] by the fraction of the molten metal excluding the additions of particles. It should be noted that Eq. [13] only gives the resistivity of the metal and cannot be used to estimate the effective resistivity within the filter media. The "effective" resistivity of the filters must be found experimentally due to the reduction in the conducting area produced by the non-conducting

ceramic filter and the increased tortuosity. Values for 30 to 80 PPI filters have been found to be 1.5 for 30 PPI, 2.5 for 40 PPI, 2.5 for 50 PPI, and 3.7 for 80 PPI, expressed as a ratio to the metal resistivity.[29]

In Figure 4, the correction factor, φ, calculated from Eq. [8], is plotted for different values of the dimensionless radius, r/R, as a function of the dimensionless reference depth at the surface, ξ_R. As can be seen from the figure, at larger values of ξ_R, a higher value is obtained for the correction factor, φ, at the surface. It can also be seen that the correction factor φ decreases rapidly with the penetration into the liquid metal.

For a fixed outer radius, R, a large dimensionless reference depth, ξ_R, corresponds to a low electromagnetic penetration depth, δ_l, and thus a high frequency, f. At high frequencies, the magnitude of Eq. [7] becomes very large at the surface (due to the low electromagnetic penetration depth obtained in the denominator as well as the high value of the correction factor, φ), and the obtained electromagnetic force becomes very powerful, but confined to a thin layer, *i.e.*, the Lorentz force boundary layer. This effect is clearly seen in Figure 5 where the time average Lorentz forces, F_{RMS}, are plotted against the dimensionless radius, r/R, for different values of the dimensionless reference depth at the surface, ξ_R, equivalent to frequencies from 16 Hz to 14.4 kHz.

III. EXPERIMENTAL

A. *Coil Specifications and Electrical Measurements*

Experiments were conducted using a flow test apparatus with two different coil designs for high and low magnetic flux densities (~0.1 and 0.2 T). For comparison, one gravity experiment was also performed in the same apparatus. Each of the coils used in the present experiments was constructed from copper tubing with 6 mm inner diameter and 1 mm wall thickness. The coils were electrically insulated using a 0.7-mm-thick high temperature glass fiber sleeve and wrapped with glass fiber tape to prevent vibration. Detailed information on the coils is summarized in Table I.

Electrical measurements (kW, kVA, V, A, and cos φ) were taken using a power analyzer from Fluke, USA (Fluke 43B), with a resolution of 0.1 kW. Current measurements were made with an inductive current probe from Fluke, USA (i1000S), with an accuracy of ±1 pct and a resolution of 1 A. The coil resistance was determined first without the liquid metal present, when operating at steady state conditions. The electrical parameters were then measured under actual test conditions with the presence of liquid metal. The net power input to the liquid metal was further determined using the measured current and the obtained change in the measured resistance.

B. *Setup*

The experimental apparatus was constructed using three lengths of BIMEX 400 fiber riser supplied by Intermet Refractory Products Ltd., U.K., with a nominal inner diameter of 102 mm, an outer diameter of ~125 mm, and a length of 150 mm. The three lengths of riser tubes were joined together using Fibrefrax® moldable cement.

In the continuous flow filtration experiments, a 30 PPI CFF was cemented into the junction of the two bottom risers, as shown in Figure 6. The coil was positioned in such a way that the mid-line of the coil and the strongest point in the magnetic field were in line with the bottom of the filter, as shown in Figures 6 and 7. The bottom section of the apparatus was glued to a 20-mm-thick ceramic alumina plate, in which a 3.2-mm hole was drilled to provide a flow control orifice. Casting sand was placed around the coil and the fiber riser tubes to ensure proper insulation of the equipment assembly and further to avoid the risk of any molten metal leakage during testing.

The temperature over and under the filter was measured using Inconel-sheathed K type thermocouples. The liquid metal flow through the filter per unit

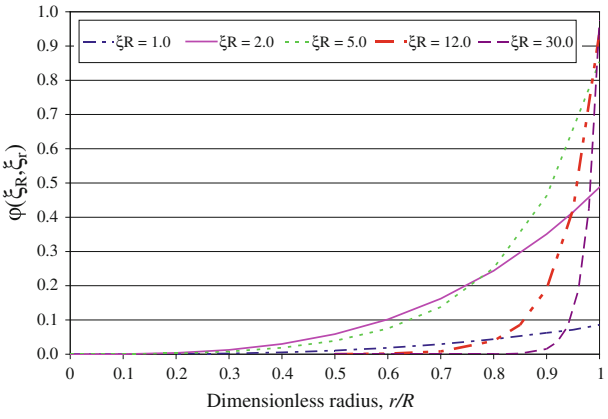

Fig. 4—The solution to Eq. [8] as a function of the dimensionless radius (r/R) for different values of the dimensionless reference depth at the surface (ξ_R).

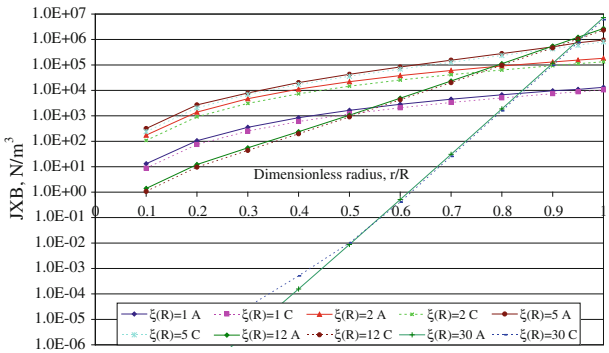

Fig. 5—Comparison of the time-averaged Lorentz force estimates from Eq. [7] and from COMSOL 4.2®. The calculations were performed for 100 mm in diameter of liquid A356 alloy (with 4 pct non-conductive solids) at 980 K (707 °C) using 932 A in a "short" coil (Coil #1).

Table I. Summary of Data for Single and Double Layer Coils

Coils	Coil #1 Single Coil	Coil #2 Double Coil
Inside diameter (mm)	126	126
Average diameter (mm)	132	140
Height (mm)	111	107
Diameter to height ratio	1.18	1.31
Coil copper tube diameter (mm)	6	6
Coil copper tube thickness (mm)	1	1
Number of turns	16.5	31.0
Measured inductance of empty coil (μH)	27.6	103.3
Measured resistance at maximum load (Ω)	0.01082	0.01962
Avg. coil temperature at maximum load [K (°C)]	316 (43)	296 (23)

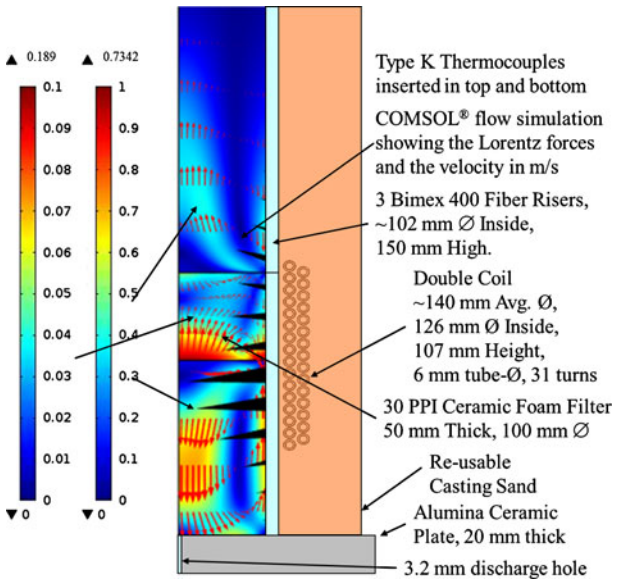

Fig. 6—A schematic drawing of the flow test apparatus with COMSOL® FEM simulation of the flow field (arrows and shading), as well as the Lorentz forces (cones), for a 30 PPI CFF in the absence of bulk flow, *i.e.*, in "batch" mode.

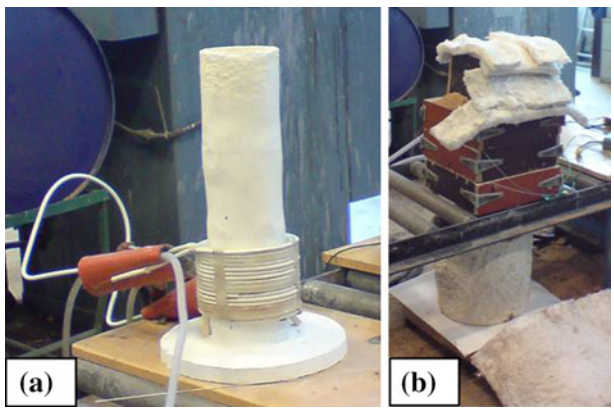

Fig. 7—Photographs of the flow test apparatus: (*a*) the double coil and fiber crucibles with alumina base plate and (*b*) the apparatus fully assembled.

time was determined by measuring the weight change as a function of time on a 100-kg scale with an accuracy of 0.01 kg. The temperature and weight values were recorded using a digital logger system.

During the experiments, metal was continuously added to maintain 250 mm of metal head over the filter. This was continued until the supply crucible (which had a capacity of 18 kg) was empty. The tests were terminated when the metal ceased to flow from the bottom orifice of the apparatus.

C. *Materials and Sample Analysis*

A standard non-grain refined A356 alloy was used for all the continuous filtration flow tests. The chemical composition of the alloy is given in Table II.

For the flow filtration tests, a feed recipe was prepared containing 60 pct A356 alloy, 20 pct anodized and lacquered plates, and 20 pct A356 composite material containing 15 wt pct SiC particles with a reported size range of 13 to 23 μm. The feed recipe alloy was melted in an induction furnace at a target temperature of 1023 K (750 °C). The melt was skimmed to remove the dross formed on the surface of the melt prior to pouring into the flow test apparatus. The dross consisted mainly of thick oxide films originating from the added anodized and lacquered plates.

For the filter element metallographic investigations, the filter media were cut into five slices using a high speed water jet. After cutting, the specimens were mounted in a cold mounted resin and further sanded using SiC-based papers (P80-P4000 Grit) to a surface finish of 5 μm. After sanding, the samples were polished using diamond suspensions with nominal grain sizes of 3 and 1 μm, each for 2 minutes with the lowest possible force on a polishing disk. Ethanol was used as a lubricant during the polishing, until a mirror-like surface finish was obtained. The hard SiC particles and soft aluminum matrix made developing a successful polishing method challenging.

The quantitative filtration efficiency for both gravity and electromagnetic field operation was determined in a second round of experiments, using 90 pct by weight A356 alloy and 10 pct by weight of the same A356 composite material containing SiC particles as used previously. A large batch of 150 kg of melt was produced in a graphite mixer-agitated resistance heated furnace for use with several experiments. The anodized

Table II. Chemical Composition of the A356 Alloy in Weight Percentage

Alloy Type	Si	Mg	Fe	Mn	Zn	Ti	Al
A356	7.03	0.41	0.091	0.008	0.005	0.11	bal

plates were eliminated due to the quantity of dross they produced and the significant loss of SiC particles that resulted. The initial quantity of SiC was reduced by 50 pct for these experiments.

Rapidly solidified metallographic samples were analyzed from before (eight samples averaged) and during the flow filtration trials (two each for gravity and electromagnetic field operation averaged, taken during the initial constant flow velocity phase). Quantitative filtration efficiency as a function of particle size has been determined using a series of digital images taken from the rapidly solidified samples. The samples were machined flat, polished to a mirror-like finish using the same procedure as for the filter sections, and optically analyzed using an LEICA MEF4M white light microscope, equipped with a Jenoptic ProgRes-C10 Plus, 10 MP digital camera. 40 pictures at 10 times magnification were taken of each sample and computer analyzed using Image-Pro® Plus Version 7.0 macro-automated image processing and analysis software. The software ran a macro to load and analyze all the pictures for each sample as a batch to determine the number and area of each individual particle and the fraction of the total area of the sample occupied by particulates.

Overall efficiency (E_{total}) could be determined by comparing the normalized count of particles (*i.e.*, particles per total area) before and after filtration.

$$E_{\text{total}} = \frac{\text{Normalized Count In} - \text{Normalized Count Out}}{\text{Normalized Count In}} \quad [14]$$

Efficiency by size ($E_{\text{size fraction } x}$) was determined using the equivalent spherical particle diameters in the ranges from 2 to 5, 5 to 10, 10 to 15, 15 to 20, and 20 to 25 μm and comparing the particle counts before and after filtration for identical photographic areas.

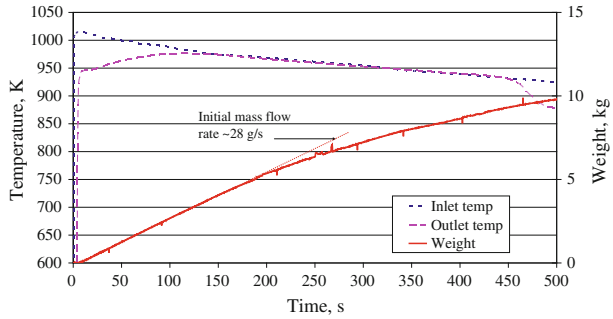

Fig. 8—Gravity test experimental data.

magnification used. Below 2 μm, "objects" like dendrites and scratches began to be counted in addition to particles.

IV. RESULTS AND DISCUSSION

The obtained results from the gravity experiment are plotted in Figure 8 and the obtained results from the experiment using the highest magnetic flux density, *i.e.*, Coil #2 at ~0.2 T, are plotted in Figure 9. As can be seen from the figures, a decrease in the feed metal temperature with time was obtained. In the case of Coil #2, however, the outlet temperature remained stable due to the resulting induction heating effects. In the case of the gravity experiment, the outlet temperature proves to have equalized with the inlet temperature, which also declined throughout the experiment. It can also be seen from Figures 8 and 9 that the discharge rates were slightly higher in the experiments performed under the influence of a magnetic field. This is believed to be due

$$E_{\text{size fraction } x} = \frac{\text{Normalized Count In}_{\text{size fraction } x} - \text{Normalized Count Out}_{\text{size fraction } x}}{\text{Normalized Count In}_{\text{size fraction } x}} \quad [15]$$

The equivalent spherical particle diameter is the spherical particle with the same area as the observed particle, correcting for the fact that the observed particle has been cut at a random "latitude" by the machining and polishing. The stereoscopic effects have been corrected by multiplying the obtained particle diameters by the average correction factor of $\sqrt{1.5}$ appropriate for spherical particles cut at a random location.[30]

Particles less than 2 μm could not be counted by this automated method with any precision for the 10 times

to thermal/viscosity effects or the magnetic pressure produced by the Lorentz forces.

All the experimental values logged during the present study are summarized in Table III. It should be pointed out that the resistivity values presented in Table III are for the metal alone and that the electromagnetic penetration depth in the metal phase has been adjusted to allow for 96 pct of the theoretic conducting area, *i.e.*, the presence of non-conducting particulates. The metal-free space velocity over the filter area was 15 mm/s in

the case of the gravity discharge and 20 mm/s in the case of the coil operation.

In Table IV, the magnitude of the Lorentz force is analytically estimated by using Eqs. [7] through [13]. The obtained results are compared to the data generated from the finite element modeling using COMSOL 4.2®. Both solutions indicate that the Lorentz forces are approximately one order of magnitude greater than the gravity forces. As a result, the Lorentz forces can be assumed to dominate the hydrodynamics of the process.

It should be pointed out that as the COMSOL 4.2® model is 2D axial symmetric, there is no exact correspondence between the geometry in the experimental setup and the model. A 17 turn coil (Coil #1) was used to model the experimental coil of 16.5 turns. In the case of the two-layered coil (Coil #2), one 16 turn layer and one 15 turn coil layer were used to model the two 15.5 turn layers of the experimental coil. For Coil #2, Eqs. [7] through [13] were numerically solved taking the average coil diameter located between the two coil layers into consideration. These equations are only valid for a single layer coil; however, this procedure has even proven to give good agreement between the calculated and measured power input (discrepancies of ±10 to 20 pct).

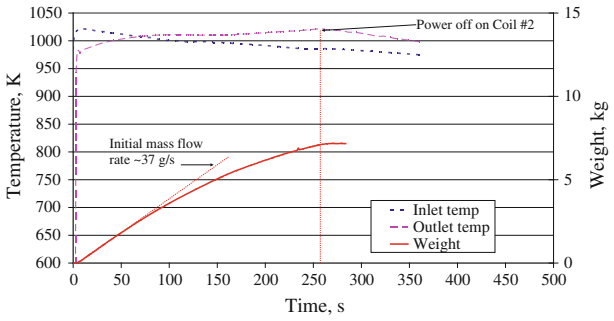

Fig. 9—High magnetic field experimental data obtained for Coil #2 at ~0.2 T, *i.e.*, the highest magnetic flux density.

In the absence of the "short" coil correction factor, *i.e.*, the result of Eq. [11], errors of more than a factor of two would be experienced in the estimated Lorentz forces using Eq. [7]. It should be noted that the Lorenz forces estimated using both COMSOL 4.2® and Eq. [7] are evaluated only at the surface, *i.e.*, radius = R, and represent an averaged or integrated value over the full height of the coil. In this comparison, the effect of the filter was excluded as Eq. [7] does not allow for variable electrical conductivity, *i.e.*, metal was assumed along the full coil height.

A representative magneto-hydrodynamic (MHD) simulation has been performed for Coil #2 using COMSOL 4.2® and is included as part of Figure 6. The flow field was calculated for the physical parameters presented in Table V. A separate article describes the careful measurement of pressure drop, Forchheimer equation[31] parameter derivations, and the filter physical characterization (porosity and effective electrical conductivity measurements) required to ensure the validity of the simulation.[29]

In Figure 6, the flow field resulting from the curl in the Lorentz forces can now be clearly seen from the arrows in the liquid metal and filter domains. The velocities in the two domains are shown by the two scale bars, indicating a maximum velocity in the liquid metal of 0.73 and 0.19 m/s in the filter media. The filter velocity is approximately one order of magnitude larger than normal velocities encountered in the gravity filtration of aluminum by CFFs, showing the dominating influence of the electromagnetic Lorentz forces on the resulting flow field.

A. *Filter Cross Sections*

In Figures 10(a) through (c), representative cross sections of the filters used during the flow tests are presented. In the case of the filtration tests performed under gravity conditions, almost no wetting is obtained in the top section of the filter, while some wetted grains

Table III. Summary of Experimental Data

Experimental Case	Voltage (V)	Current (A)	Power (kW)	Net Power (kW)	Average Temperature [K (°C)]	Equation [13] Estimated Metal Resistivity (Ω m)	Equation [10] Feed Recipe 8 (mm)
Coil #1	13.30	932	10.0	0.8	980 (707)	3.02E−07	39.9
Coil #2	28.58	715	12.7	1.8	1005 (732)	3.06E−07	40.2
Gravity	N/A	N/A	0	0	959 (686)	N/A	N/A

Table IV. Comparison of Calculated Lorentz Force Estimates from Analytical Equations and COMSOL 4.2®

Experimental Case	Equation [11] Short Coil Correction Factor (unitless)	Calculated Average Air-Gap Flux Density (T)	Equation [9] ξ_R and ξ_r at Surface (Unitless)	Equation [8] φ (Unitless)	Equation [7] Lorentz Forces at Surface (kN/m^3)	COMSOL Estimate of Lorentz Force (kN/m^3)
Coil #1	0.725	0.126	1.77	0.351	−111	−93
Coil #2	0.697	0.181	1.76	0.351	−229	−182
Gravity	N/A	0	N/A	N/A	0	0

Table V. Summary of Data Used in FEM Flow Field Simulation

Model Criteria	Value	Units	References
Forchheimer Darcy term, k_1	5.08	10^{-8} m^2	[29]
Forchheimer non-Darcy term, k_2	5.46	10^{-4} m	[29]
Filter total porosity, ε	0.892	Unitless	[29]
Liquid metal density, ρ	2390	kg/m^3	[46]
Liquid metal viscosity, μ	1.0	mPa S	[47]
σ_{metal}-containing particles	3.14	MS/m	[28]
Filter resistance ratio, $\sigma_{filter}/\sigma_{metal}$	1.5	Unitless	[18]
Current, I	715	A	—
Frequency, f	50	Hz	—
Coil	#2	—	—

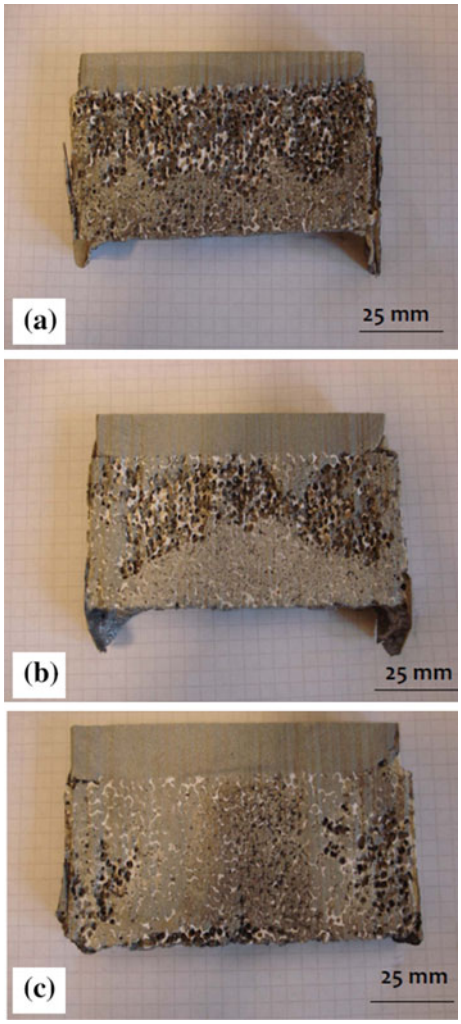

Fig. 10—Filter cross sections from flow tests performed under different experimental conditions, *i.e.*, (*a*) gravity, (*b*) low magnetic flux density (Coil #1), and (*c*) high magnetic flux density (Coil #2).

are observed at the bottom section, see Figure 10(a). Even from the filtration tests performed with low magnetic flux density (Coil #1 at ~0.1 T), non-wetted grains are obtained at the top section of the filter, but complete wetting is observed at the bottom section, see Figure 10(b). Filter grains are completely wetted by the molten metal when performing the filtration tests with high magnetic flux density (Coil #2 at ~0.2 T), see Figure 10(c). The presented cross sections clearly demonstrate the effect that the magnetic field strength has on the molten metal when filtered through a conventional non-conductive filter media.

B. *Particle Distribution Inside the Filter*

In Figures 11 to 14(a) through (c), representative optical micrographs resulting from gravity flow tests and high magnetic flux density tests, using Coil #2 at ~0.2 T, are presented. As can be seen from Figures 11(a) and 12(a), the filter cake is intact and dense in the case of the gravity filtration test, while the cake is disrupted and less dense in the case of filtration under the influence of a electromagnetic field. It can also be seen from the figures that there are more SiC particles present on top of the filter in the sample poured under gravity conditions, while the SiC particle density is less in the sample poured and stirred with the electromagnetic field. Under gravity conditions, there is clearly no wetting of the filter grains in the central regions of the filter, while complete wetting is obtained in the case of filtration combined with a "strong" electromagnetic field. Another observation is that more particulates are found at the bottom of the gravity filtration sample, see Figure 11(c), compared with the bottom of the electromagnetically stirred sample, see Figure 12(c). This is believed to be due to the "strong" upward flow located in the central part of the filter, as shown in Figure 6.

C. *Filter Side Wall*

In Figures 13 and 14(a) through (c), the comparison between the SiC particle distributions inside the filter media and along the filter side walls for the gravity flow test, as well as the high magnetic flux density test with Coil #2 at ~0.2 T, is presented. As can be seen from the micrographs, the wetting conditions are visibly improved by the application of the electromagnetic field during filtration. It is, however, qualitatively observed that the number of particles collected along the filter side wall in the gravity filtration experiment is less than in the case of the filtration combined with the electromagnetic forces. It is believed that particles are transported and

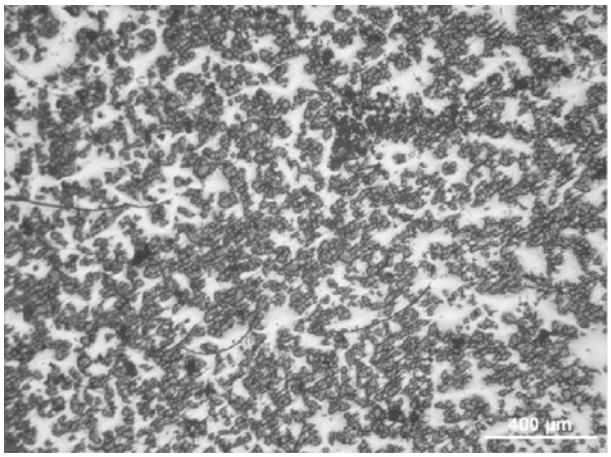

(a) Top

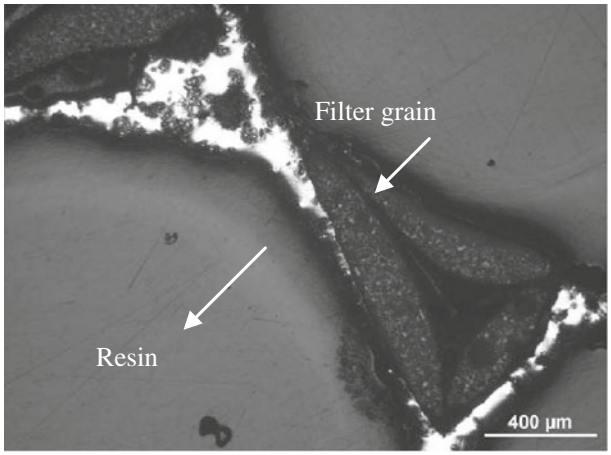

(b) Middle

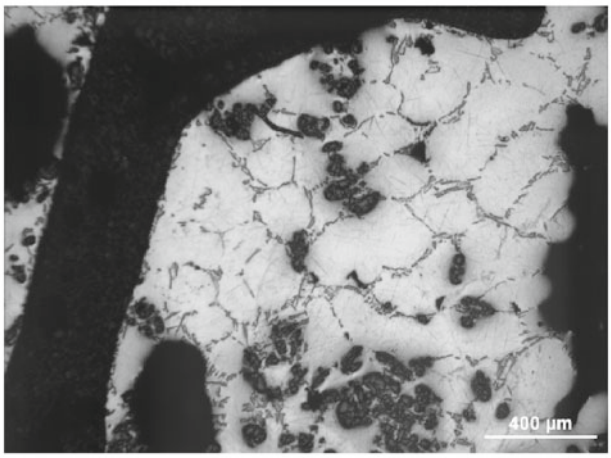

(c) Bottom

Fig. 11—The SiC particle distribution, inside the filter media along the filter center line, resulting from the gravity flow tests. The overall direction of flow is from the top to the bottom of the figure. The magnification for each of the micrographs is 50 times.

collected at the filter side wall as a direct result of the strong upward fluid circulation through the filter center and the downward circulation along the side wall, caused by the strong curl present in the Lorentz forces, as shown in Figure 6.

D. *Quantitative Filtration Efficiency*

The Image-Pro® Plus Version 7.0 software successfully counted the areas of >93 pct (when compared against a meticulous manually controlled count) of the individual particles from each micrograph for sizes >2 μm. Representative initial and final micrographs are shown in Figures 15(a) through (c). The adjusted equivalent spherical particle diameters have been measured for each sample and assembled into histograms of particle count in and out for both the gravity and the electromagnetic experiment using Coil #2, as shown in Figures 16(a) and (b).

The overall filtration efficiencies for both the gravity (0.844) and the electromagnetic filtration experiment (0.472) have been calculated using Eq. [14], and the results have been plotted against "typical" results for the same type of 30 PPI commercial filters in Figure 17. The obtained overall filtration efficiencies are found to both be within the wide range of expected performance for this type of commercial filter. The gravity result is located very near the maximum and the electromagnetic result is toward the average of the "typical" values. Given that both are within the normal range, it is difficult to reach a firm conclusion, although the preliminary data appear to indicate a decrease in the overall filtration efficiency for the electromagnetic experiment.

Empirical models of filtration proposed for this type of CFF are of the following form[32]:

$$E_{\text{size fraction } x} = 1 - e\left(\frac{-K_0 L}{V_f}\right) \qquad [16]$$

where $E_{\text{size fraction } x}$ is the fractional collection efficiency of size fraction, x, based on observed particle counts in and out using Eq. [15]; K_0 is an empirical constant (1/s) for each range of sizes, having reported values of[32] 0.205 for 15 to 20 μm, 0.250 for 20 to 25 μm, and 0.283 for 25 to 30 μm particles; L is the filter thickness (mm); and V_f is the interstitial velocity of the melt within the filter (mm/s). Typically, K_0 is determined from LiMCA data in and out and such data are not available for sizes <15 μm due to limitations in the measuring principle applied.

Based on Eq. [16], it would be expected that individual and overall filtration efficiency will vary inversely proportionally to the aluminum "casting" rate in the range of typical velocities from 3 to 19 mm/s.[32] The high efficiency found for the gravity filtration experiment is likely explained by the fact that a low interstitial velocity on the order of 2 mm/s was used when compared with typical filtration velocities.

The low efficiency of the electromagnetic experiment could also be expected in light of Eq. [16] and the extremely high flow velocities induced by the curl in the electromagnetic Lorentz forces inside the filter region, *i.e.*, 10 to 189 mm/s, as shown previously in Figure 6. The higher melt velocities may have broken internal "bridges," which typically form during deep filtration in CFFs as shown in Figure 18,[32] or re-entrained material collected at the walls and hence elutriated previously collected particles from the filter.

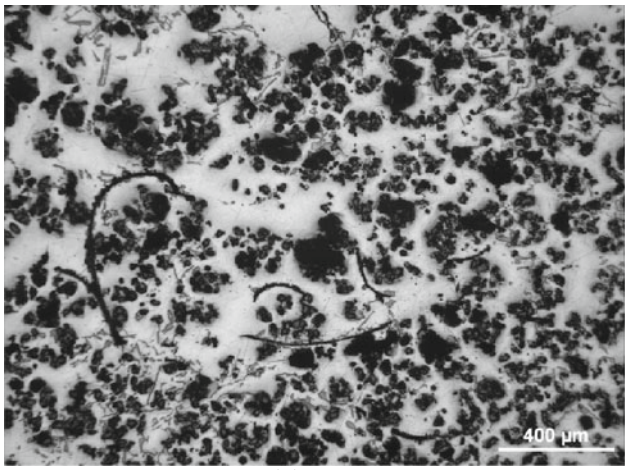

(a) Top

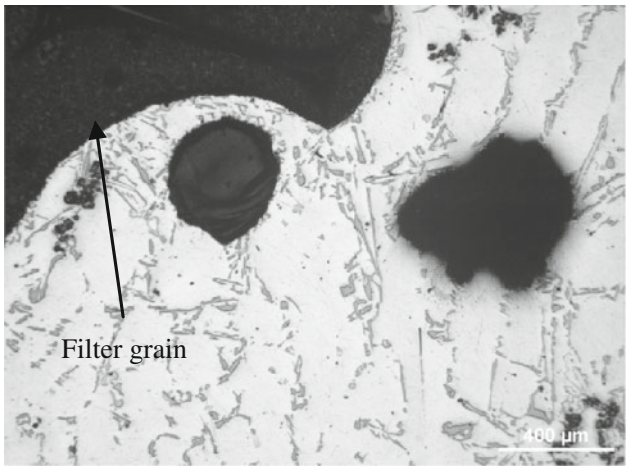

(b) Middle

(c) Bottom

Fig. 12—The SiC particle distribution, inside the filter media along the filter center line, resulting from a high magnetic flux density test (Coil #2 at 0.2 T). The overall direction of flow is from the top to the bottom of the figure. The magnification for each of the micrographs is 50 times.

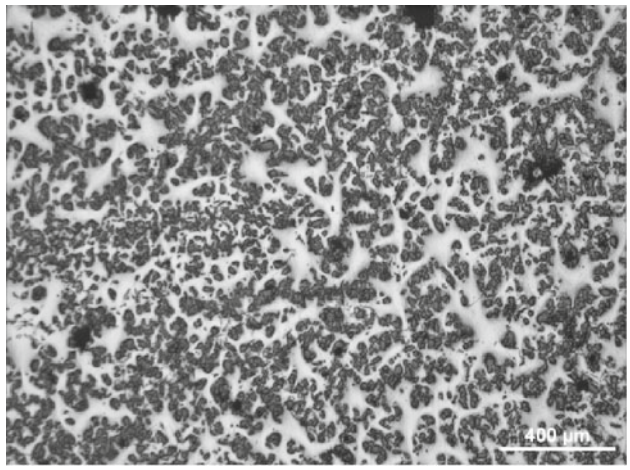

(a) Top

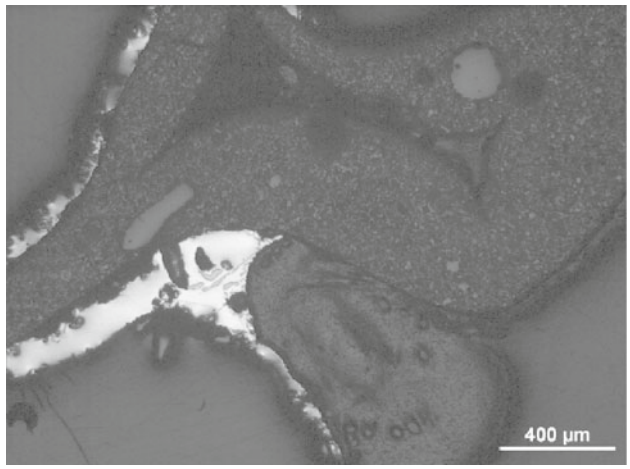

(b) Middle

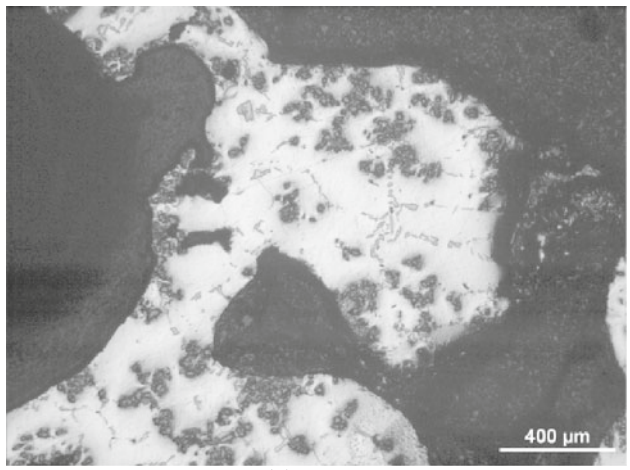

(c) Bottom

Fig. 13—The SiC particle distribution, inside the filter media along the filter side wall, resulting from gravity flow tests. The overall direction of flow is from the top to the bottom of the figure. The magnification for each of the micrographs is 50 times.

If the fine nature of the particles used in this experiment is taken into account, Eq. [16] would indicate that the overall observed electromagnetic filtration efficiency (0.472) is representative of a bulk velocity of about 12 mm/s. Given that the actual range of velocities induced by the Lorentz forces was up to 15 times higher,

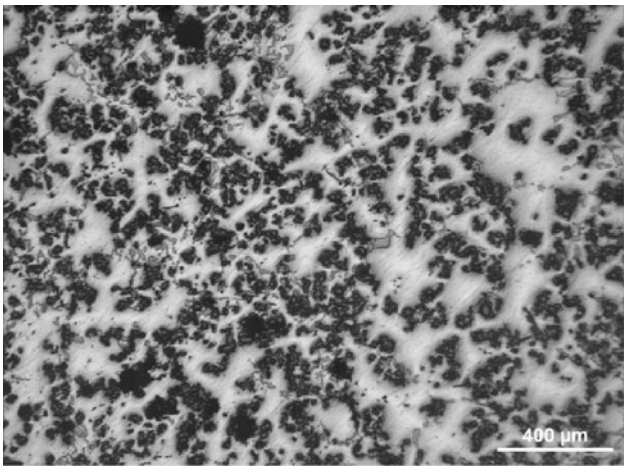

(a) Top

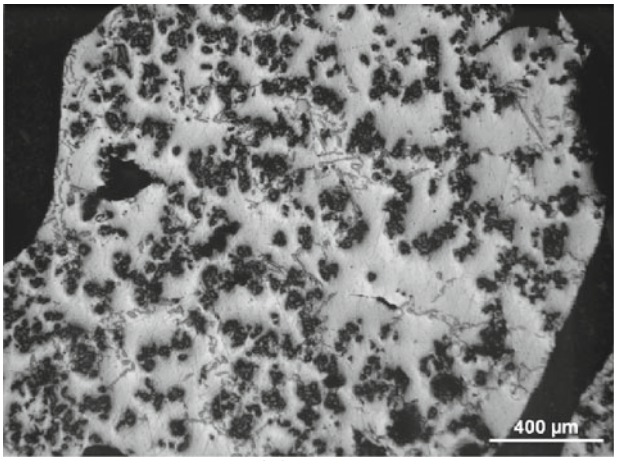

(b) Middle

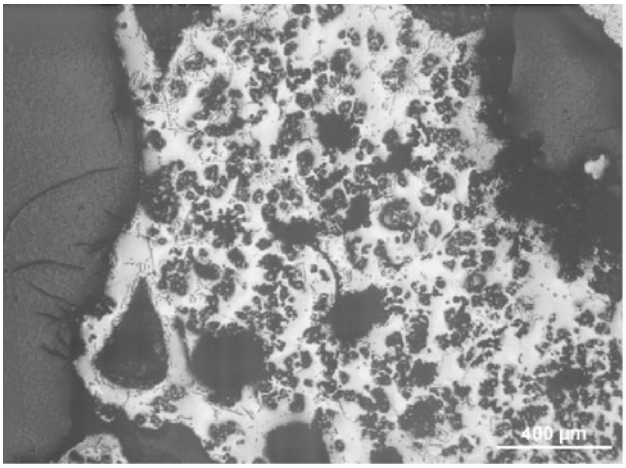

(c) Bottom

Fig. 14—The SiC particle distribution, inside the filter media along the filter side wall, resulting from the high magnetic flux density test (Coil #2 at 0.2 T). The overall direction of flow is from the top to the bottom of the figure. The magnification for each of the micrographs is 50 times.

this could indicate that bulk recirculation of the melt driven by the Lorentz forces or "enhanced" removal by the *Leenov-Kolin "pinch" effect* in the hydrodynamic boundary layer at the sides of the filter may have had a compensating effect. More optimized results might be experienced by testing alternate filters with different permeability, utilizing a different magnetic flux density or alternate coil configurations (*e.g.*, variable pitch), producing different magnitudes and curls of the Lorentz forces.

Particle efficiency by size has been calculated for both the gravity and the electromagnetic filtration experiments using Eq. [15] and plotted in Figure 19. Results indicate that each experiment has both different overall efficiencies and also substantially different variation of efficiency as a function of particle size. In the case of gravity filtration, the efficiency is relatively constant, increasing slightly with particle size in the size range of 2 to 25 μm. In the case of the electromagnetic experiment, the filtration efficiency decreases monotonously with increasing particle size. An examination of the micrographs presented in Figures 11 through 15 indicates a high degree of agglomeration of individual particles. It may be that particle agglomerates are formed (during the master alloy solidification or during remelting) and can be subsequently collected, with some common efficiency, rather than as individual particles being collected with differing efficiencies. In Figure 20, a typical "cluster" or agglomerate from the "cleaned" side of the electromagnetic filtration experiment is shown. Expanded bifilms are often observed decorated with numerous particles over, inside, and under the filters.[33] Bifilms appear to play a role as a "scaffold," building bridges across the open windows within the filter porosity and may play a role in the overall filtration efficiency, as has been described in previous investigations.[34]

The decrease of efficiency with increasing size in the case of the electromagnetic filtration may be due either to greater re-entrainment at the high velocities induced by the electromagnetic Lorentz forces or more likely due to rapid settling of the largest particles once they have made their "first pass" through the filter, *i.e.*, large particles and agglomerates are more likely to settle once below the filter and not have a second or third chance at "re-filtration" due to bulk fluid recirculation as shown in Figure 6. The decrease in efficiency with increased particle size is a strong indication that bulk recirculation and not the *Leenov-Kolin effect* is "maintaining" the overall efficiency at these high interstitial velocities during the electromagnetic filtration.

Clustering or agglomeration effects with SiC[35,36] as well as other particles, such as intermetallics[37] and TiB_2,[38] have been reported many times in the literature. These clustering effects lead to rapid settling of particulates in liquid aluminum, at rates about an order of magnitude higher than would be expected from the Stokes law. Stokes law is only valid for freely falling individual particles. This rapid particle settling was also observed during batch testing conducted as part of this study.[33] It is hypothesized that these clustering effects dominate the filtration efficiency of particles in the size ranges used in this study, which would invalidate models based on single particle efficiency and negate the value of so-called "particle tracking" using MHD-FEM.

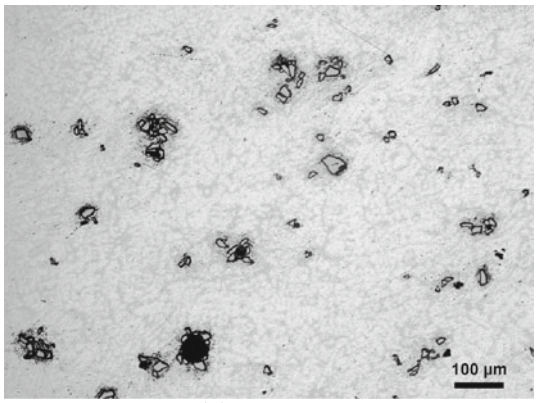

(a) before filtration

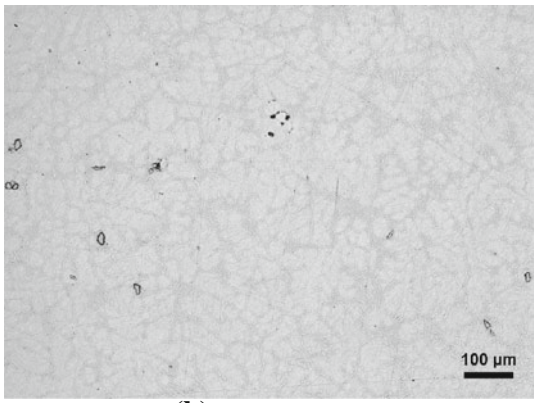

(b) after gravity filtration

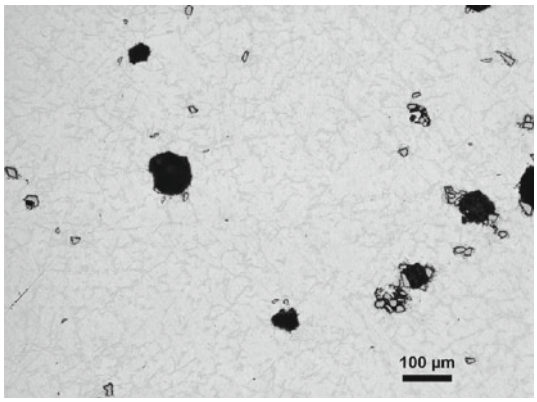

(c) after electromagnetic filtration

Fig. 15—Representative micrograph (*a*) before and (*b*) after gravity and (*c*) electromagnetic filtration at ~0.2 T, taken at 10 times magnification with a light microscope.

Cluster effects emerge in processes when the particle density becomes high enough (highly likely just over or inside of a filter), or the level of turbulence becomes large enough, for particles to have a high probability of "encountering" and interacting with one another, for example to minimize their net surface energy. These "particles" can be liquid organic media in solvent extraction mixer-settlers, liquid metal prills in molten slag containing furnaces, or even solid particles in gas-particle cyclones. These effects have become better known within particle-gas physics for highly loaded cyclones, where particles at and below 1 μm can be collected with extremely high efficiency when cyclones are operated with high inlet loadings due to clustering.[39] These solid "clusters" are not broken up in such cyclones, even with many gs of gravity force, so it is further hypothesized that the clusters encountered in the

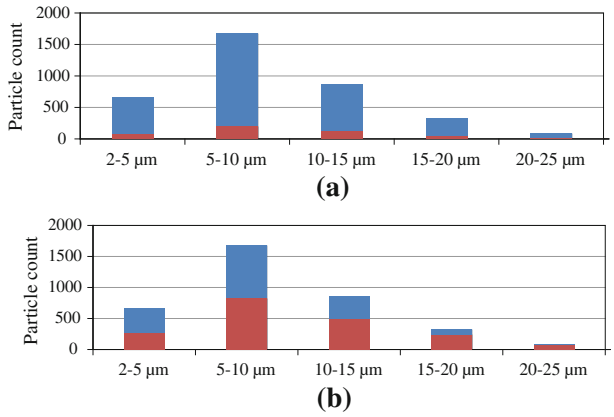

Fig. 16—Particle counts in and out for (*a*) 30 PPI gravity and (*b*) electromagnetic filtration experiments as functions of size ranges from 2 to 25 μm, at ~0.2 T.

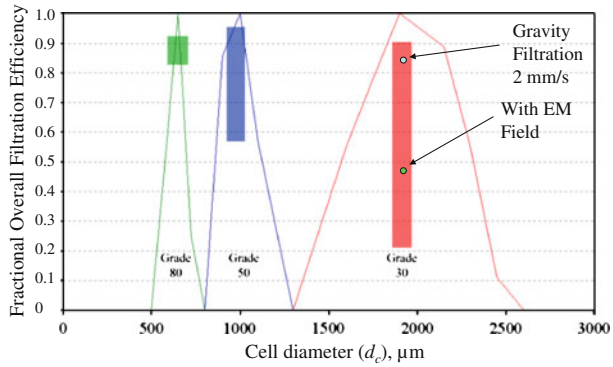

Fig. 17—Overall filtration efficiency for 30 PPI gravity and electromagnetic experiments, plotted *vs* "typical" industrial filter performance, for the same type of commercial filters.[42]

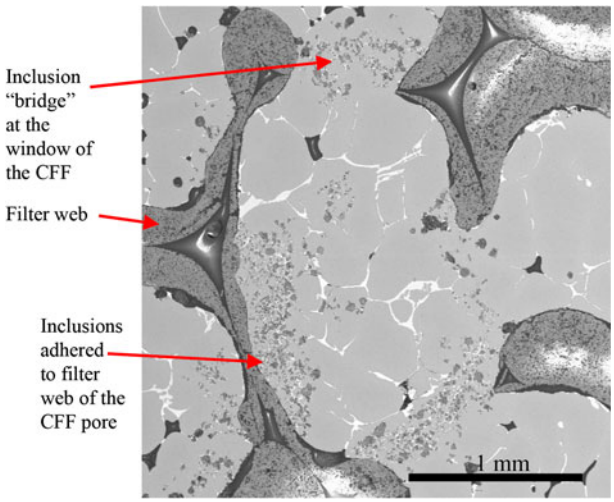

Fig. 18—Particle bridges formed during filtration of aluminum.[32]

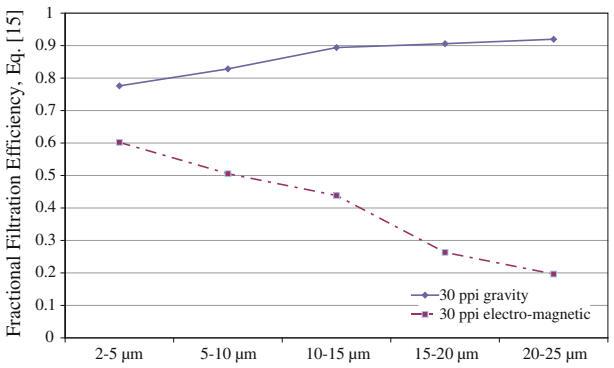

Fig. 19—Filtration efficiency as a function of particle size range from 2 to 25 μm for 30 PPI gravity and electromagnetic experiments at ~0.2 T.

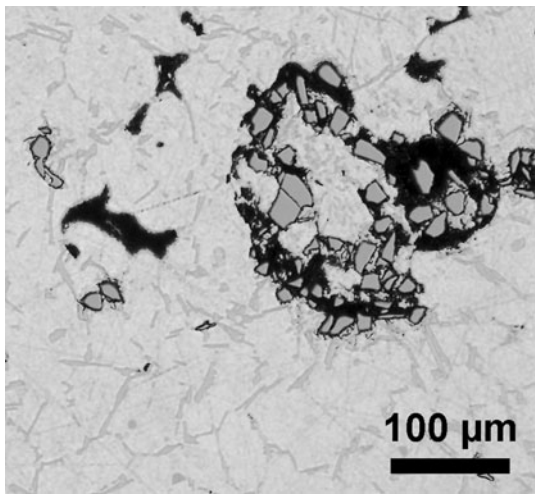

Fig. 20—SiC Agglomerates found in the "cleaned" metal taken from the outlet of the 30 PPI electromagnetic filtration apparatus.

current experiment will not be deagglomerated by the mixing effects induced by the curl of the Lorentz forces.

Previous publications could not be found giving filtration efficiency by size in aluminum for the range of particles used in this study, as the industry standard LiMCA equipment has difficulty to accurately detect particles below 20 μm.[34,40–42] The macro-automated computerized optical analysis technique used in this study may offer a reasonable way to explore the efficiency of filtration for very fine particles in molten metal processes.

V. CONCLUSIONS

The powerful mixing caused by the curl in the Lorentz force fields (produced by "short" induction coils) has a profound impact on the wetting behavior and resulting distribution of SiC particles during filtration of liquid aluminum using CFFs. In the case of electromagnetic stirring, fewer particles have been found on top of the filter, and more particles were located close to the side walls of the crucible. The higher velocities induced inside the filter by the influence of the Lorentz forces appear to have resulted in a reduction in the overall filtration efficiency from 0.844 to 0.472, for the 30 PPI commercial CFFs used in this study, and a significant change in the variation of the particle filtration efficiency with size.

The filtration efficiencies have been reported as a function of size using a macro-automated computerized optical analytical procedure suitable for very fine particulates from 2 to 25 μm. The observed efficiency of filtration for the very fine particulates used in these experiments was higher than expected (*e.g.*, 0.844 for gravity) and did not appear to vary substantially as a function of particle size under gravity filtration conditions. Clustering effects appear to create agglomerates of fine particles, which are subsequently collected with high and nearly uniform filtration efficiency. This would not be possible to measure using industrial measuring devices of the LiMCA type as agglomerates would be counted as individual "large" particles.

A new analytical expression for the time-averaged Lorentz forces has been proposed, incorporating a frequency modified "short" coil correction factor which shows good agreement with estimates found using finite element modeling (COMSOL 4.2®).

VI. FURTHER WORK

In order to better understand and optimize the electromagnetically modified filtration process, the physical (permeability at high velocity and porosity) and electrical conductivity properties of CFFs must be combined into a MHD model of the type shown in Figure 6. The physical and electrical properties of CFFs from 30 to 80 PPI have been measured, modeled analytically and using CFD, and reported in a separate article.[29]

The obtained efficiency for gravity and electromagnetic filtration, using 30 to 80 PPI filters at both low and high bulk filtration velocities, has been measured and will be reported in a future publication.[43] Results are compared with flow fields computed with MHD modeling using validated filter properties and with representative micrographs.

Practical implications of the current research on the design and operation of cast house filter equipment and a detailed description of the optical analysis technique are to be published in future articles.[44,45]

ACKNOWLEDGMENTS

The present study was carried out as part of the RIRA (Remelting and Inclusion Refining of Aluminium) project funded by the Norwegian Research Council (NRC)—BIP Project No. 179947/I40. The industrial partners involved in the project are Hydro Aluminium AS, SAPA Heat Transfer AB, Alcoa Norway ANS, the Norwegian University of Science and Technology (NTNU), and SINTEF Materials and Chemistry. The funding granted by the industrial partners and the

NRC is gratefully acknowledged. The authors wish to express their gratitude to Egil Torsetnes at the NTNU for helping with the design and construction of the experimental apparatus. Sincere gratitude is also due to Kurt Sandaunet at SINTEF for his support and help as well as for the use of the SINTEF laboratory. The high quality metallographic work of Robert Fritzsch and Behzad Mirzaei was also invaluable.

REFERENCES

1. S. Makarov, R. Ludwig, and D. Apelian: *Meas. Sci. Technol.*, 1999, vol. 10, pp. 1047–53.
2. Z. Xu, T. Li, and Y. Zhou: *Metall. Mater. Trans. A*, 2007, vol. 38A, pp. 1104–10.
3. T. Li, Z. Xu, B. Sun, D. Shu, and Y. Zhou: *Acta Metall. Sinica Engl. Lett.*, 2000, vol. 13, pp. 1068–74.
4. L. Damoah and L. Zhang: *Metall. Mater. Trans. B*, 2010, vol. 41B, pp. 886–907.
5. D. Leenov and A. Kolin: *J. Chem. Phys.*, 1954, vol. 22, pp. 683–88.
6. P. Vilinskas and R. Schiltz: *Nucl. Appl.*, 1969, vol. 6 (2), p. 176.
7. C. Conti, J. Meyer, J. Riquet, and P. Netter: Patent Number EP 290360 A(00290360/EP-A), 1988.
8. D. Shu, T. Li, B. Sun, J. Wang, and Y. Zhou: *Metall. Mater. Trans. A*, 1999, vol. 30A, pp. 2979–88.
9. K. Takahashi and S. Taniguchi: *ISIJ Int.*, 2003, vol. 43, pp. 820–27.
10. J.P. Park, A. Morihira, K. Sassa, and S. Asai: *Tetsu-to-Hagané*, 1994, vol. 80, p. 389.
11. S. Taniguchi and J. Brimacombe: *ISIJ Int.*, 1994, vol. 34, pp. 722–31.
12. J. Barglik and C. Sajdak: *Elektrowärme Int.*, (2), 1985, pp. B77–B80.
13. D. Shu, B. Sun, K. Li, J. Wang, and Y. Zhou: *ISIJ Int.*, 2002, vol. 42, pp. 1241–50.
14. N. El-Kaddah, A. Patel, and T. Natarajan: *JOM*, 1995, vol. 47, pp. 46–49.
15. N. El-Kaddah: US Patent 4,909,836, 1990.
16. D. Shu, J. Wang, H. Chen, and B. Sun: US Patent Application 20,080/216,601, 2005.
17. M.W. Kennedy, S. Akhtar, J.A. Bakken, and R.E. Aune: *Light Metals*, San Diego, California, 27 February–3 March, 2011, pp. 763–68.
18. R. Fritzsch, M.W. Kennedy, S. Akhtar, J.A. Bakken, and R.E. Aune: *Electromagnetic Processing of Materials*, Beijing, China, 23–25 October, 2012, pp. 1–4.
19. M.W. Kennedy, S. Akhtar, J.A. Bakken, and R.E. Aune: *EPD Congress*, San Diego, California, 27 February–3 March, 2011, pp. 707–22.
20. M.W. Kennedy, S. Akhtar, J.A. Bakken, and R.E. Aune: *COMSOL Users Conference*, Stuttgart, Germany, 26–28 October, 2011, pp. 1–9.
21. M.W. Kennedy, S. Akhtar, J.A. Bakken, and R.E. Aune: *Light Metals*, Orlando, FL, 11–15 March, 2012, pp. 269–75.
22. R. Weaver: http://electronbunker.ca/DL/NumericalExamples01.ods, accessed 15 December 2012.
23. N. McLachlan: *Bessel Functions for Engineers*, Clarendon Press, Gloucestershire, 1955, pp. 215–30.
24. V. Korovin: *Magnetohydrodynamics (Engl. Transl.)*, 1986, vol. 22, pp. 17–19.
25. V. Korovin: *Magnetohydrodynamics (Engl. Transl.)*, 1986, vol. 21, pp. 321–26.
26. H. Nagaoka: *J. Coll. Sci.*, 1909, vol. 27, pp. 18–33.
27. D. Knight: *Part 1: Solenoid Inductance Calculation*, October, 2012, http://www.g3ynh.info/zdocs/magnetics/Solenoids.pdf, accessed 15 December 2012.
28. R. Brandt and G. Neuer: *Int. J. Thermophys.*, 2007, vol. 28, pp. 1429–46.
29. M.W. Kennedy, K. Zhang, R. Fritzsch, S. Akhtar, J.A. Bakken, and R.E. Aune: *Metall. Trans. B*, 2012 (accepted).
30. A. Çiftja: PhD Thesis, Department of Materials Science and Engineering, NTNU, Trondheim, 2009.
31. P. Forchheimer: *Z. Ver. Deutsch. Ing.*, 1901, vol. 45, pp. 1782–88.
32. S. Ray, B. Milligan, and N. Keegan: *Aluminium Cast House Technology 2005*, 9th Australasian Conference and Exhibition, Melbourne, Australia, 12–15 September, 2005, pp. 1–12.
33. R. Fritzsch: Masters Thesis, Department of Materials Science and Engineering, NTNU, Trondheim, 2011.
34. H. Duval, C. Rivière, É. Laé, P. Le Brun, and J. Guillot: *Metall. Mater. Trans. B*, 2009, vol. 40B, pp. 233–46.
35. A. Kolsgaard and S. Brusethaug: *Mater. Sci. Eng. A*, 1993, vol. 173, pp. 213–19.
36. A. Ourdjini, K. Chew, and B. Khoo: *J. Mater. Process. Technol.*, 2001, vol. 116, pp. 72–76.
37. S. Shabestari and J. Gruzleski: *Metall. Mater. Trans. A*, 1995, vol. 26A, pp. 999–1006.
38. P.L. Schaffer and A.K. Dahle: *Mater. Sci. Eng. A*, 2005, vol. 413, pp. 373–78.
39. A. Hoffmann, H. Arends, and H. Sie: *Filtr. Sep.*, 1991, vol. 28, pp. 188–93.
40. D. Chesonis, D. DeYoung, D. Lake, N. Ridler, G. Alcoa Manufacturing, L.W. Works, and W.S.A.I. Swansea: *Light Metals*, Seattle, 17–21 February, 2002, pp. 937–44.
41. N. Keegan, W. Schneider, and H. Krug: *Light Metals*, San Diego, California, 28 February–4 March, 1999, pp. 1031–41.
42. N.J. Keegan and S.F. Ray: in *Alcastek*, Mumbai, India, Dr. Nilmanied, ed., 2002, pp. 1–10.
43. M.W. Kennedy, R. Fritzsch, S. Akhtar, J.A. Bakken, and R.E. Aune: *Metall. Trans. B*, 2012 (in press).
44. R. Fritzsch, M.W. Kennedy, J.A. Bakken, and R.E. Aune: *Light Metals*, San Antonio, 3–7 March, 2013 (in press).
45. R. Fritzsch, B. Mirzaei, M.W. Kennedy, J.A. Bakken, and R.E. Aune: *Light Metals*, San Antonio, 3–7 March, 2013 (in press).
46. K. Yeum and D. Poirier: *Light Metals*, 1988, pp. 469–76.
47. D. Wang and R. Overfelt: *Int. J. Thermophys.*, 2002, vol. 23, pp. 1063–76.